

Significant Increase of Electron Thermal Conductivity in Dirac Semimetal Beryllonitrene by Doping Beyond Van Hove Singularity

Zhen Tong,* Alessandro Pecchia, ChiYung Yam, Hua Bao, Traian Dumitrică,* and Thomas Frauenheim*

2D beryllium polynitrides or beryllonitrene is a newly synthesized layered material displaying anisotropic Dirac cones and van Hove singularity (VHS) located only ≈ 0.5 eV above the Fermi level. Using the Boltzmann transport equation with many-body effects and first-principles calculations, it is uncovered that beryllonitrene has an in-plane anisotropic room-temperature phonon thermal conductivity (κ_{ph}) of 78.6 and 98.8 W mK⁻¹, and an electron thermal conductivity (κ_{e}) of 23.0 and 60.7 W mK⁻¹, along the in-plane directions. κ_{ph} is dominated by the large heat capacity flexural acoustic (ZA) modes, which are susceptible to three-phonon and four-phonon scatterings but rather immune to scattering onto electrons. Filling the Dirac cones till VHS and above gradually enhances the phonon–electron coupling and monotonically decreases κ_{ph} by up to 55%. Instead, κ_{e} displays unusual nonmonotonic variations with the increase in the carrier density and follows the electron density of states at corresponding Fermi levels. The results shed light on the thermal and electrical transport properties in beryllonitrene and reveal a thermal conductivity modulation mechanism that includes a 60% increase of κ_{e} upon filling of the Dirac cones until VHS.

1. Introduction

Determining the properties of 2D matter in the one-atom-thin limit is a current frontier of science.^[1–18] One such emergent quantum phenomenon is the electronic transport through Dirac cones, which were first identified in graphene.^[1–3] Close to the charge neutrality point, the graphene dispersion relation is linear and well described by the relativistic Dirac equation^[4] with charge


carriers as massless Dirac fermions. The Dirac fermions in graphene display a large spectrum of phenomena, such as ultrahigh carrier mobility,^[1–3] quantum Hall effects,^[5] quantum transport,^[6] and Klein tunneling.^[7] At ≈ 2 eV above the Dirac point,^[4] graphene displays a VHS, which is essentially a nonsmooth point in the electronic density of states (el-DOS). Doping graphene to VHS and beyond is a challenging task and accessing the large number of available VHS states is actively pursued^[9,10] in order to access a strong many-body interactions regime.

Although thermal properties of 2D materials are intensely investigated,^[11–13,16–27] less is known about thermal conductivity of 2D Dirac materials^[28] especially the impact of VHS on the energy carrier (electron and phonon) transport properties. High-pressure technologies demonstrated great potential^[29] for enriching the variety of 2D Dirac materials, which are rare compared with the

numerous 2D materials.^[30] Bykov et al.^[29] recently demonstrated high-pressure synthesis of one-atom-thick BeN₄ layers, called beryllonitrene, consisting of metal atoms connecting zigzag nitrogen chains. Notably, *ab initio* calculations^[29,31,32] provided compelling evidence for Dirac cones of the Fermi level. Bafekry et al.^[31] found Dirac cones configuration in monolayer and bilayer BeN₄, while structures thicker than three-layers were shown to develop metallic character. Mortazavi et al.^[32] predicted the anisotropic Dirac cone

Z. Tong, C. Y. Yam, T. Frauenheim
Shenzhen JL Computational Science and Applied Research Institute
Shenzhen 518131, China
E-mail: tongzhen@csar.ac.cn

Z. Tong, C. Y. Yam, T. Frauenheim
Beijing Computational Science Research Center
E-mail: Beijing 100193, China

 The ORCID identification number(s) for the author(s) of this article can be found under <https://doi.org/10.1002/adfm.202111556>.

© 2022 The Authors. Advanced Functional Materials published by Wiley-VCH GmbH. This is an open access article under the terms of the Creative Commons Attribution-NonCommercial-NoDerivs License, which permits use and distribution in any medium, provided the original work is properly cited, the use is non-commercial and no modifications or adaptations are made.

DOI: 10.1002/adfm.202111556

A. Pecchia
CNR-ISMN
Via Salaria Km 29.300, Monterotondo, Rome 00017, Italy

H. Bao
University of Michigan-Shanghai Jiao Tong University Joint Institute
Shanghai Jiao Tong University
Shanghai 200240, China

T. Dumitrică
Department of Mechanical Engineering
University of Minnesota
Minnesota 55455, USA
E-mail: dtraian@umn.edu

T. Frauenheim
Bremen Center for Computational Materials Science
University of Bremen
2835 Bremen, Germany
E-mail: thomas.frauenheim@bccms.uni-bremen.de

electronic structure. Notably, these studies revealed VHS located closer to the Fermi level, making it more accessible through n doping than in graphene. While these recent investigations studied the electronic, mechanical, optical properties, the thermal properties of the new Dirac semimetal material remained unexplored.

In this work, we determine the total thermal conductivity ($\kappa_{\text{total}} = \kappa_{\text{ph}} + \kappa_{\text{e}}$) in beryllonitrene with a theoretical framework that combines the first-principles calculations and the solution of the Boltzmann transport equation (BTE).^[27,33–35] The model includes a spectrum of many body interactions: intrinsic three-phonon (3ph) and four-phonon (4ph) scatterings^[27,33] as well as the extrinsic phonon-limited^[34,35] scattering including phonon–electron (ph-el) and phonon–isotope (ph-iso). It provides both κ_{ph} and κ_{e} thermal conductivities. n -doped beryllonitrene was also considered in order to investigate the potential impact of the Dirac states on κ_{total} . The BTE calculations for doped beryllonitrene reveal distinct roles for the electron–phonon coupling and electronic density of states on κ_{ph} and κ_{e} and the ability of the Dirac fermions to modulate the intra-layer heat transfer.

2. Results and Discussion

2.1. Electronic and Phononic Band Structures

Figure 1a shows the optimized lattice structure of beryllonitrene, in which the BeN_4 “molecule” is repeated in a parallelogram lattice crystal (a $p2$ 2D space group). The computed electronic band structure, total and projected electron density-of-states (el-DOS) are shown in Figure 1b. As it can be seen in the projected el-DOS, the electronic states around the Fermi level originate in the p_z orbitals of nitrogen. As recognized by Bykov et al.,^[29] the linear dispersion in the vicinity of the Fermi energy indicates the Dirac semimetal character of beryllonitrene, while graphene presents Dirac points at the high symmetry point of the Brillouin zone (BZ), beryllonitrene’s cones are centered at the Σ -points, between Γ and A_1 points. Their location inside the BZ is shown in Figure 1c. The off-symmetry position of Dirac points is a signature of the lower lattice symmetry of the one-atom-thick BeN_4 .^[29,32]

The distinct slopes of the Dirac cone along Σ – Γ and Σ – A_1 are indicating the anisotropic character of the carrier velocities. Note that the anisotropy is also visible in the Fermi contours (yellow lines) shown in Figure 1c. Using $v(\mathbf{k}) = 1/\hbar[\partial E(\mathbf{k})/\partial \mathbf{k}]$, we obtained the Fermi velocity $v_x = 2.75 \times 10^5 \text{ m s}^{-1}$ along Σ – A_1 and $v_y = 7.34 \times 10^5 \text{ m s}^{-1}$ along Σ – Γ . Our values agree well with literature data such as $v_x = 3.0 \times 10^5 \text{ m s}^{-1}$ ($v_y = 8.0 \times 10^5 \text{ m s}^{-1}$) in ref. [29] and $v_x = 2.92 \times 10^5 \text{ m s}^{-1}$ ($v_y = 7.46 \times 10^5 \text{ m s}^{-1}$) in ref. [32]. The large Fermi velocities originated from the Dirac cone are expected to drive high carrier mobilities, as it was observed in graphene,^[5] where the Fermi velocity measures $1.1 \times 10^6 \text{ m s}^{-1}$.^[5]

Although the Dirac cone spans a $\approx 2 \text{ eV}$ energy range, a first VHS arises at about 0.5 eV above the Fermi level due to the flat conduction band at Y. This is notably different from graphene, where the VHS–Fermi level separation is $\approx 2 \text{ eV}$. We conjecture that through doping, reaching the first VHS in beryllonitrene should be less challenging than in graphene. Indeed, the shifting of the Fermi energy by 0.5 eV in graphene is possible through chemical doping,^[36] and by 2 eV and above by gadolinium intercalation,^[9] and by ytterbium intercalation combined with potassium adsorption methods.^[10] While the low el-DOS in vicinity of the Fermi level in intrinsic beryllonitrene are indications for a weak el-ph coupling, the strong Fermi surface nesting features in doped beryllonitrene are expected to strengthen the el-ph coupling and thus to impact thermal transport.

Figure 1d presents the calculated phononic band structure. The lack of any imaginary frequency confirms the stability of beryllonitrene. As in graphene, we obtain that the out-of-plane acoustic (ZA) phonon modes displays a quadratic dependence on \mathbf{q} near the zone center of BZ (Γ point), while the acoustic in-plane transverse (TA) and longitudinal (LA) modes are both linear in \mathbf{q} .

2.2. κ_{total} in Intrinsic Beryllonitrene

The results of our κ_{ph} and κ_{e} calculations (in-plane averaged) are shown in Figure 2a. While at 300 K, thermal transport is mainly phononic with κ_{ph} of 78.6 W mK^{-1} (along x) and 98.8 W mK^{-1} (along y), the electronic contribution with κ_{e} of 23.0 W mK^{-1}

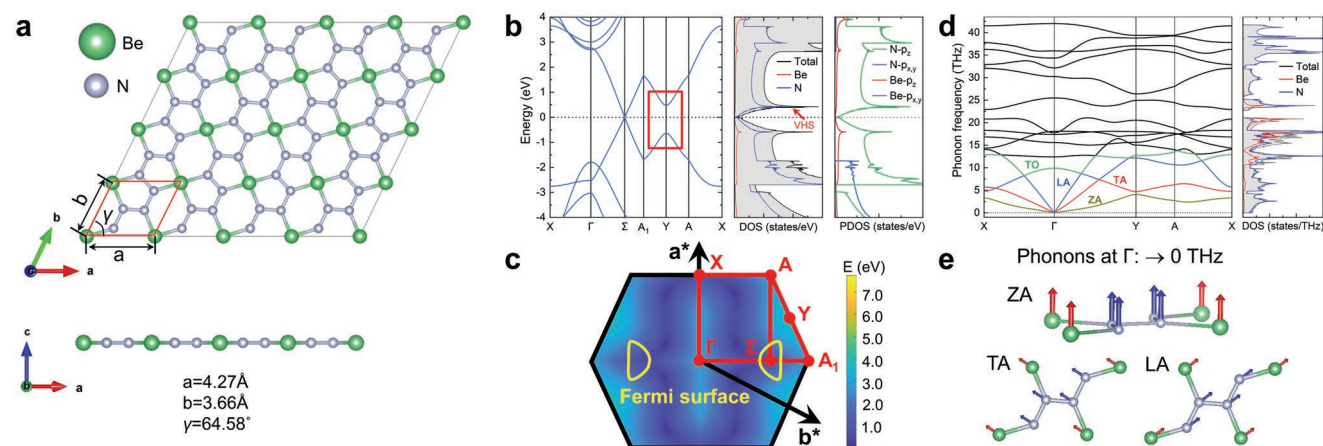


Figure 1. a) Top and side view of beryllonitrene. The primitive unit cell consists of 1 Be atom and 4 N atoms. b) Electronic band structure with the corresponding total and projected electron density-of-states. The zero of energy is set to the Fermi level. c) Contour plot of the electronic energy dispersion in the Brillouin zone of beryllonitrene, with Σ labeling the Dirac point. d) Phonon dispersion with the corresponding total and projected phonon density-of-states. The TA, LA, ZA, and one transverse optical (TO) phonon modes are labeled. e) Vibrational pattern of TA, LA, ZA phonon modes near Γ point.

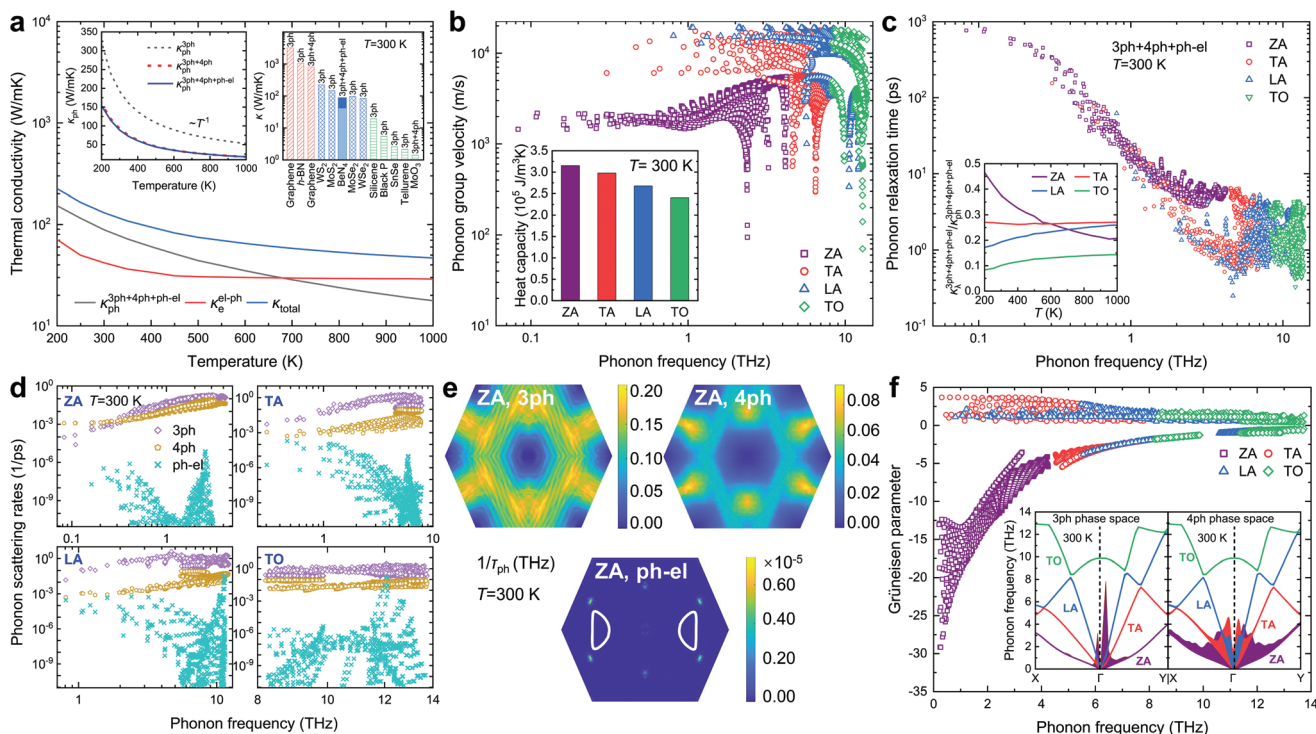


Figure 2. a) κ_{ph} , κ_{e} , and κ_{total} of intrinsic beryllonitrene versus T . Superscripts denote inclusion of 3ph, 3ph+4ph, and 3ph+4ph+ph-el scattering events. The left inset is the variation of κ_{ph} with T of the different scattering terms. The right inset summarizes literature data (theoretical) for the $T = 300$ K thermal conductivity of other 2D materials: graphene,^[19,25] h-BN,^[22] 2D WS_2 and MoS_2 ,^[20] 2D MoSe_2 and WSe_2 ,^[20] silicene,^[23] phosphorene,^[23] SnSe,^[24] tellurene,^[26] and 2D MoO_3 .^[27] b) Phonon group velocity of ZA, TA, LA, and TO modes. The inset is the corresponding volumetric heat capacity at $T = 300$ K. c) Phonon relaxation time of ZA, TA, LA, and TO modes at $T = 300$ K. The inset is their normalized contributions to κ_{ph} . d) The 3ph, 4ph, and ph-el scattering rates at $T = 300$ K. e) The contour plot of 3ph, 4ph, and ph-el scattering rates of ZA modes at $T = 300$ K. f) Grüneisen parameters. The inset is the weighted phonon phase space for 3ph and 4ph scattering processes at $T = 300$ K. The weighted phonon phase space (unit in ps^4/rad^4 for 3ph and ps^5/rad^5 for 4ph)^[33,37] is shown with a variable-width band on the phonon dispersion branch.

(along x) and 60.7 W mK^{-1} 41.88 W mK^{-1} (along y) is non-negligible as it brings a $\approx 30\%$ to the total thermal conductivity κ_{total} . The temperature-dependent κ_{ph} and κ_{e} along x and y directions are shown in Figure S5, Supporting Information. With the increase in temperature (T), κ_{ph} follows a T^{-1} dependence while κ_{e} remains practically constant. The latter behavior is consistent with the low el-DOS available for thermal electrons in vicinity of the Fermi energy. Above the crossover $T = 700$ K, κ_{total} is dominated by the electronic carriers. The right inset of Figure 2a places our result in the context of other important 2D materials. The $T = 300$ K predicted κ_{total} places beryllonitrene in the intermediate range, in between MoS_2 and MoSe_2 , indicating a robust capability of spreading heat in potential quantum devices.

As in graphene^[19,25] and 2D MoO_3 ,^[27] here we find that the ZA modes are important for phononic transport. Figure 2b plots for ZA, TA, LA, and TO modes their phonon group velocity and heat capacity in the corresponding inset. The ZA modes bring an important contribution due to their large heat capacity originating in the low phonon frequency range. This can be seen from Figure 2c, where the computed $\tau_{\text{ph}}^{3\text{ph}+4\text{ph}+\text{ph-el}}$ for ZA is larger than that of TA, LA, and TO modes. The inset in Figure 2c shows ZA modes contribute $\approx 40\%$ to κ_{ph} at $T = 300$ K.

For more insights, the left inset of Figure 2a presents separately the different contributions to κ_{ph} . Accounting only for the 3ph scatterings in $\kappa_{\text{ph}}^{3\text{ph}}$ leads to a significant overpredictions at all T .

The usually neglected 4ph term brings an important contribution, suggesting that the narrow range of phonon frequency shown in Figure 1d provides enough phonons to satisfy the energy and momentum conversion for 4ph interactions. The ph-el component turns out to be negligible as the $\kappa_{\text{ph}}^{3\text{ph}+4\text{ph}}$ and $\kappa_{\text{ph}}^{3\text{ph}+4\text{ph}+\text{ph-el}}$ curves practically overlap, which is due to the much smaller ph-el scattering rates compared to 3ph+4ph scattering as shown in Figure 2c.

The relative importance of the 3ph, 4ph, and ph-el, scattering events emerges by quantitatively comparing the different scattering rates of ZA, TA, LA, and TO modes, in Figure 2c,d. On one hand, we find that for ZA the 3ph scatterings are comparable to the 4ph ones, a behavior that doesn't hold for other modes (TA, LA, and TO). Given the importance of the ZA modes for heat transport, this finding is consistent with the reduction of $\approx 50\%$ reduction from $\kappa_{\text{ph}}^{3\text{ph}}$ to $\kappa_{\text{ph}}^{3\text{ph}+4\text{ph}}$ at $T = 300$ K, see the inset in Figure 2c. On the other hand, the ph-el scattering rates are quite small compared to the 3ph and 4ph scattering rates, especially for those modes in vicinity of zone center shown in Figure 2e. Thus, the electron-phonon coupling is weak in intrinsic beryllonitrene, a result that is consistent with the low contribution to κ_{ph} of the ph-el component.

The strength of the ph-ph scattering is reflected in the anharmonic interaction matrix elements and the inverse of phonon phase space.^[33,37] Anharmonicity can be generally measured by the Grüneisen parameter γ ^[33] which quantifies the volume

change with T . Figure 2f shows our calculated γ for all acoustic and TO modes. The large γ of ZA implies stronger anharmonicity compared to other modes, thus predominately limiting the finite κ_{ph} . The phonon phase space reflects all available phonon scattering processes for simultaneously satisfying the energy and momentum conservation. The inset in Figure 2f shows the weighted phonon phase space^[33,37] of ZA, TA, LA, and TO, confirming abundant scattering channels for the ZA modes.

2.3. κ_{total} in n -Doped Beryllonitrene

We next considered thermal transport in n -type beryllonitrene with carrier concentration (n) ranging from 0.6×10^{13} to $138 \times 10^{13} \text{ cm}^{-2}$, reaching beyond the VHS. Prior to the production calculations we have verified our implementation in n -doped graphene, see Section S4, Supporting Information. As shown in Figure S6e, Supporting Information, our results agree well with the available experimental and theoretical data, demonstrating the reliability of our approach.

Figure 3a shows that the κ_{total} versus n of beryllonitrene at $T = 300 \text{ K}$ exhibits an unusual nonmonotonic dependence on n . This behavior does not originate in the κ_{ph} , which was shown to dominate thermal transport in intrinsic beryllonitrene, but in the variations of κ_{e} with n . We discuss next these two components.

κ_{ph} presents a monotonous decrease, which becomes more pronounced only when doping beyond VHS. The reduction reaches $\approx 55\%$ at $n = 138 \times 10^{13} \text{ cm}^{-2}$, similar to the behavior observed earlier in doped silicon^[38] and 2D Dirac silicene.^[39] The decreasing trend is the outcome of the increased scattering of phonons onto electrons. As confirmed in Figure 3b, the ph-el scattering rate increased with n : While for the intrinsic case, $1/\tau^{\text{ph-el}}$ is much smaller than $1/\tau^{\text{3ph+4ph}}$, they become comparable at $n = 138 \times 10^{13} \text{ cm}^{-2}$. Further supporting this conclusion, we find that the transport electron-phonon coupling strength $\lambda_{\text{tr}} = 0.06$ (see definition in Section S5, Supporting Information) for intrinsic beryllonitrene is much smaller than $\lambda_{\text{tr}} = 0.54$ of n -type beryllonitrene with $n = 138 \times 10^{13} \text{ cm}^{-2}$ (Figure S7, Supporting Information).

κ_{e} of beryllonitrene imparts the nonmonotonic dependence with n seen in κ_{total} and remarkably, follows the shape of el-DOS, shown by a green shade in Figure 3a. With respect to the κ_{e} of intrinsic beryllonitrene, κ_{e} increases by up to 60% at $n = 16.71 \times 10^{13} \text{ cm}^{-2}$ (at the VHS), while the maximum reduction reaches 70% at $n = 55.02 \times 10^{13} \text{ cm}^{-2}$. Such strong correlation between κ_{e} and el-DOS in beryllonitrene obtained with BTE is approximately captured by Drude's free electron model,^[40] $\kappa_{\text{e}}^{\text{Drude}} = \pi^2/3k_{\text{B}}^2TN_{\text{F}}v_{\text{F}}^2\tau$, where k_{B} is the Boltzmann constant, N_{F} is the Fermi DOS per spin and per unit cell, v_{F} is the Fermi velocity, and $\tau = 12 \text{ fs}$ the electron lifetime (See Figure S8, Supporting Information), which was taken to be on the order of magnitude of electron lifetimes in metals.^[41]

It is interesting to relate the obtained κ_{e} variations to the el-ph rate and electron group velocity changes with n . Figure 3c displays the computed $1/\tau_{\text{ik}}^{\text{el-ph}}$ and electron group velocity (v_{ik}) variations with energy at three representative n values. When n changes from 1.06×10^{13} to $16.71 \times 10^{13} \text{ cm}^{-2}$, v_{ik} increases with n while $1/\tau_{\text{ik}}^{\text{el-ph}}$ practically remains unchanged. This is also reflected by the averaged electron lifetime $\langle\tau_{\text{e}}^{\text{el-ph}}\rangle$ and group

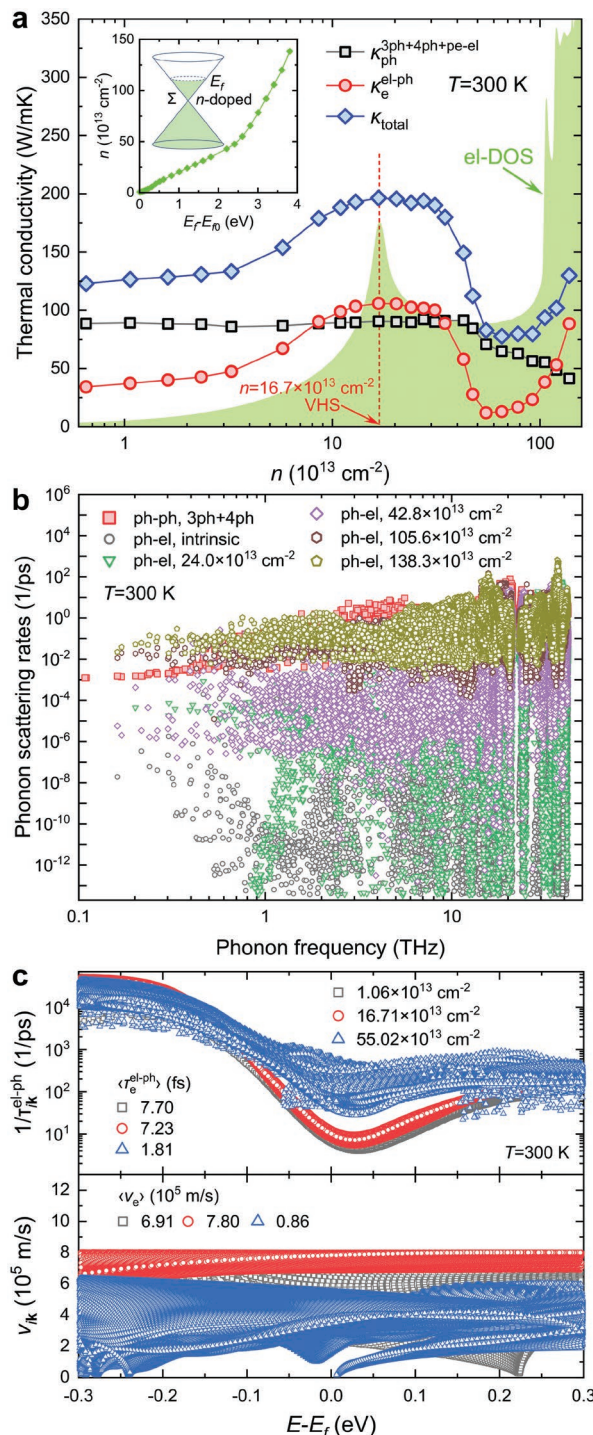


Figure 3. a) κ_{ph} , κ_{e} , and κ_{total} at room temperature vary with carrier concentration of n -type beryllonitrene. The green shaded area is the el-DOS. The inset is the variation of carrier density n with shifted Fermi energy $E_{\text{F}} - E_{\text{F}0}$ ($E_{\text{F}0}$ is the Fermi energy of intrinsic beryllonitrene) in which an inset shows the enlargement of the Dirac cones in n -type beryllonitrene and the conduction band is partly filled by electrons shown as green shading. b) Calculated phonon scattering rates of intrinsic ph-ph scattering (3ph + 4ph) as well as ph-el scattering for intrinsic and n -doped with different concentration in beryllonitrene at $T = 300 \text{ K}$. c) Calculated electron scattering rates and group velocity of n -type beryllonitrene. The averaged electron lifetime $\langle\tau_{\text{e}}^{\text{el-ph}}\rangle$ and group velocity $\langle v_{\text{e}} \rangle$ are presented in the plots.

velocity $\langle v_e \rangle$ (see the definitions in Section S6, Supporting Information) shown in Figure 3c. Thus, the increase of κ_e when doping up to the VHS can be related to the group velocity changes. When n changes from 16.71×10^{13} to $55.02 \times 10^{13} \text{ cm}^{-2}$, both $\tau_{ik}^{\text{el-ph}}$ and v_{ik} are decreasing, thus leading to the decrease of κ_e with n , Figure 3a. Thus, the subsequent lowering of κ_e is related to both of the lowering of the group velocity and the increase in electron-phonon scatterings.

To our knowledge, the modulation of κ_e through a n -doping of the Dirac cone mechanism until VHS and beyond has not been reported before. It is well known that the carrier doping leading to the Fermi energy shift will tune the electron-phonon^[18,38,42] coupling effects on the energy carrier (electron and phonon) thermal transport. While that the effect of carrier doping on the electrical transport properties of graphene has been investigated earlier,^[36,43–46] in these previous works the magnitude of the Fermi energy shift did not reach the elevated VHS. As shown in Figure S6d, Supporting Information, with our mode-by-mode ab initio analysis that calculates κ_e based on BTE (see Equation (S17), Experimental Section), we were able to obtain el-DOS shaped variation of κ_e versus n in graphene as well. The considered shift in the Fermi energy was up to 2.2 eV (larger than the separation energy of the VHS in graphene of 2 eV).

2.4. Electrical Mobility and Mean Free Paths

Electric resistivity is an important property for the potential applications in electronics. In this respect, we have calculated the phonon-limited electrical resistivity $\rho = 1/\sigma$ and mobility $\mu = \sigma/ne$ (where σ is the electrical conductivity, e is the elementary charge, and n is the charge carrier density) at different n . The results are shown in Figure 4a. Our predictions in general agree with the calculations carried out with the Allen's model (see Equation (S23) in Section S8, Supporting Information), which obviously validates our implementation. We find that ρ of beryllonitrene is larger than that of graphene at comparable n , indicating a weaker electrical transport ability. The calculated $543.59 \text{ cm}^2 \text{ V}^{-1} \text{ s}^{-1}$ and $1565.54 \text{ cm}^2 \text{ V}^{-1} \text{ s}^{-1}$ along the in-plane directions at $n = 2.34 \times 10^{13} \text{ cm}^{-2}$ ($T = 300 \text{ K}$) are much smaller than that of graphene ($5000 \text{ cm}^2 \text{ V}^{-1} \text{ s}^{-1}$ at 300 K). Compared with some other 2D materials illustrated in the inset of Figure 4a, beryllonitrene is classified as a 2D materials with $\mu_e \approx 1000 \text{ cm}^2 \text{ V}^{-1} \text{ s}^{-1}$, indicating the excellent potential applications in quantum devices.

Our κ_{total} calculations may motivate experimental measurements.^[54,55] The mean free paths (Λ) of the energy carriers are of importance for practical device design considerations and thus we have computed them. A computed accumulation function (see the definition in Section S9, Supporting Information), which generally describes the energy carrier contributions to thermal transport, is shown in Figure 4b for both electron and phonon at $T = 300 \text{ K}$. We can see that the dominant contributions to κ_{total} is brought by phonons with Λ between 10–1000 nm and electrons contribute to the κ_e with Λ ranging in 100–1000 nm. Thus, beryllonitrene samples with sizes larger than 100 nm must be considered in order to capture the nanoscale heat transport via both electrons and phonon carriers.

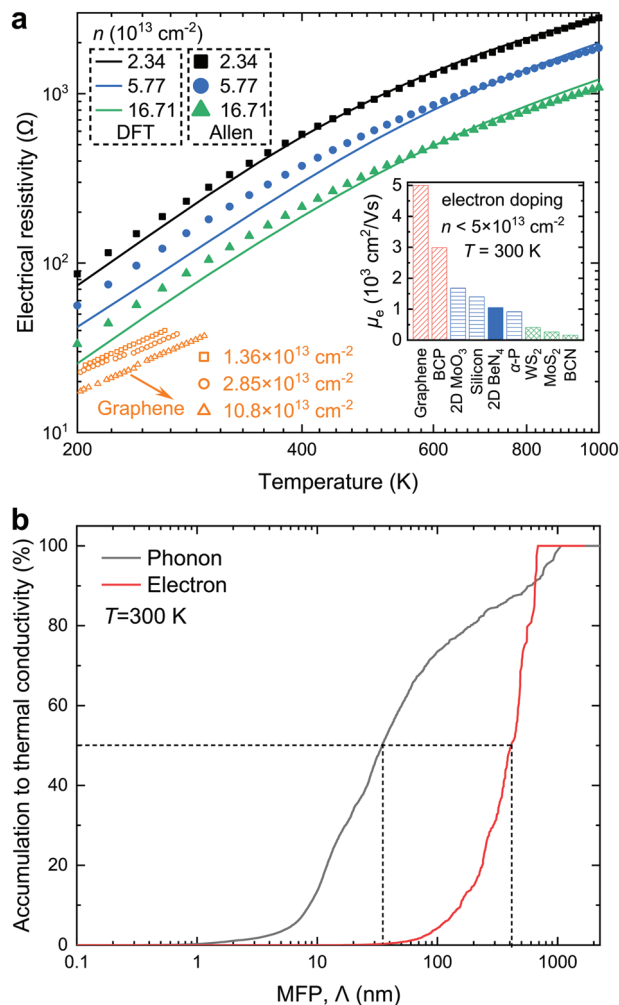


Figure 4. a) Calculated electrical resistivity of n -type beryllonitrene varies with T , which are compared with the data calculated by Allen's model.^[47,48] The available data of electrical resistivity of graphene^[36,45] are also plotted for comparison. The inset is electron mobility of some typical single-layer 2D materials and bulk silicon^[49] at $T = 300 \text{ K}$. The data are sorted by descending mobility values. Literature data for graphene,^[3] α -Phosphorene,^[50] 2D MoO_3 ,^[51] 2D WS_2 , and MoS_2 ,^[46] and borocarbophosphide (BCP) and borocarbonitride (BCN).^[52,53] b) Accumulation to thermal conductivity of phonon (κ_{ph}) and electron (κ_e) in intrinsic beryllonitrene vary with Λ at $T = 300 \text{ K}$.

3. Conclusion

Using a theoretical framework that combines BTE with first-principles calculations, we conducted a comprehensive study predicting $\kappa_{\text{total}} = \kappa_{\text{ph}} + \kappa_e$ of beryllonitrene, a 2D Dirac semi-metal with VHS close to the Fermi level. At room temperature, thermal transport is dominated by κ_{ph} through the ZA modes, which are susceptible to 3ph and 4ph scatterings but rather immune to scattering onto electrons. Upon the filling of the Dirac cones to VHS and above, the phonon–electron coupling is gradually enhanced, a behavior that impacts differently κ_{ph} and κ_e : κ_{ph} undergoes a monotonic decrease, which becomes more significant only at doping above VHS. With a still weak electron-phonon coupling, κ_e undergoes a $\approx 60\%$ increase around VHS (at $n \approx 16 \times 10^{13} \text{ cm}^{-2}$) followed by a decrease by up to 70%, above VHS (at $n \approx 55 \times 10^{13} \text{ cm}^{-2}$). These

nonmonotonic variations follow the complex shape of the el-DOS in the vicinity of the Fermi level. Our work sheds light on understanding the thermal conductivity in intrinsic and doped beryllonitrene and reveals a mechanism for manipulating electronic thermal transport specific to 2D semimetals with VHS located closely to the Fermi level.

4. Experimental Section

Utilizing BTE and the Fourier's law of heat conduction, the elements of the phononic thermal conductivity tensor can be written as^[56]

$$\kappa_{\text{ph}}^{\alpha\beta} = \frac{1}{N_{\text{q}}V} \sum_{\lambda} \hbar \omega_{\lambda} \frac{\partial n_{\lambda}^0}{\partial T} \nu_{\lambda,\alpha} \nu_{\lambda,\beta} \tau_{\lambda}^{\text{ph}} \quad (1)$$

Here, N_{q} is the total number of q-points sampled in the first Brillouin zone, V is the volume of the unit cell, \hbar is the reduced Planck constant, ω_{λ} is the frequency of phonon mode $\lambda = (\mathbf{q}, \nu)$ with polarization ν and wave vector \mathbf{q} , n_{λ}^0 is the Bose–Einstein distribution function, T is temperature, $\nu_{\lambda,\alpha}$ is the α component of the phonon group velocity, and $\tau_{\lambda}^{\text{ph}}$ is the phonon relaxation time. With the Matthiessen's rule^[56]

$$\frac{1}{\tau_{\lambda}^{\text{ph}}} = \frac{1}{\tau_{\lambda}^{\text{3ph}}} + \frac{1}{\tau_{\lambda}^{\text{4ph}}} + \frac{1}{\tau_{\lambda}^{\text{ph-iso}}} + \frac{1}{\tau_{\lambda}^{\text{ph-el}}} \quad (2)$$

in the phonon scattering rate ($1/\tau_{\lambda}^{\text{ph}}$) the intrinsic 3ph ($1/\tau_{\lambda}^{\text{3ph}}$) and 4ph ($1/\tau_{\lambda}^{\text{4ph}}$) scatterings as well as for extrinsic ph-el ($1/\tau_{\lambda}^{\text{ph-el}}$) and ph-iso ($1/\tau_{\lambda}^{\text{ph-iso}}$) scatterings were accounted for, which were all ab initio computed. More details of the derivations of the scattering rates are provided in Section S1.1, Supporting Information.

The electronic thermal conductivity $\kappa_{\text{e}}^{\alpha\beta}$ was derived instead by combining BTE and the Onsager relations^[56] and took a form that is similar with Equation (1), see Section S1.2, Supporting Information of the SM. $\kappa_{\text{e}}^{\alpha\beta}$ accounts for the electron–phonon (el-ph) $1/\tau_{\mathbf{k}}^{\text{el-ph}}$ scattering rate, which was also computed here in ab initio manner. Here \mathbf{k} is the electronic wave vector and i the band index.

Density functional theory and density functional perturbation theory (DFPT) calculations carried out with the VASP^[57] package were used to compute the ph-ph scattering rates. The Perdew–Burke–Ernzerhof exchange and correlation functionals^[58] were employed with the projector-augmented wave method. The $1/\tau_{\lambda}^{\text{3ph}}$ and $1/\tau_{\lambda}^{\text{ph-iso}}$ were calculated using ShengBTE,^[33] and the $1/\tau_{\lambda}^{\text{4ph}}$ were computed using an in-house code.^[27,59,60] With QUANTUM ESPRESSO,^[61] the electron–phonon coupling matrix elements were calculated using DFPT with norm-conserving pseudopotentials^[62] and generalized gradient approximation exchange and correlation functional^[58]. The calculations initially carried out on a coarser $18 \times 18 \times 1$ k-points (electron) and $6 \times 6 \times 1$ q-points (phonon) for the wave vector grids, were followed by calculations on finer $200 \times 200 \times 1$ k-points and $50 \times 50 \times 1$ q-points grids. To compute the $1/\tau_{\mathbf{k}}^{\text{ph-el}}$, the maximally localized Wannier functions basis, were used as implemented in the electron–phonon Wannier (EPW) package.^[63,64] To calculate the electron–phonon scattering rates $1/\tau_{\mathbf{k}}^{\text{el-ph}}$, fine $500 \times 500 \times 1$ k-points and $200 \times 200 \times 1$ q-points grids were employed. An in-house modified EPW code^[35,65,66] was used to predict the electron–phonon coupling scattering rates in order to efficiently compute the fine k- and q-point grids. Additional simulation details and convergence tests are provided in Sections S2 and S3, Supporting Information, respectively.

Supporting Information

Supporting Information is available from the Wiley Online Library or from the author.

Acknowledgements

The authors would like to thank Dr. Shouhang Li for valuable discussions. T.F. acknowledges support from DFG FR-2833/7 and National Natural Science Foundation of China (Grant No. U1930402). Z.T. acknowledges the support by National Natural Science Foundation (Grant No. 52106068), China Postdoctoral Science Foundation (Grant No. 2020M680127), Guangdong Basic and Applied Basic Research Foundation (Grants Nos. 2020A1515110838 and 2021A1515011688), and Shenzhen Science and Technology Program (Grant No. RCBS20200714114919142). Simulations were performed at the Tianhe2-JK of Beijing Computational Science Research Center.

Open access funding enabled and organized by Projekt DEAL.

Conflict of Interest

The authors declare no conflict of interest.

Data Availability Statement

The data that support the findings of this study are available from the corresponding author upon reasonable request.

Keywords

2D materials, beryllonitrene, density functional theory, doping, thermal conductivity

Received: November 12, 2021

Revised: December 15, 2021

Published online: January 12, 2022

- [1] K. S. Novoselov, *Science* **2004**, 306, 666.
- [2] K. S. Novoselov, A. K. Geim, S. V. Morozov, D. Jiang, M. I. Katsnelson, I. V. Grigorieva, S. V. Dubonos, A. A. Firsov, *Nature* **2005**, 438, 197.
- [3] A. K. Geim, K. S. Novoselov, *Nat. Mater.* **2007**, 6, 183.
- [4] A. H. Castro Neto, F. Guinea, N. M. R. Peres, K. S. Novoselov, A. K. Geim, *Rev. Mod. Phys.* **2009**, 81, 109.
- [5] Y. Zhang, Y.-W. Tan, H. L. Stormer, P. Kim, *Nature* **2005**, 438, 201.
- [6] Y.-W. Son, M. L. Cohen, S. G. Louie, *Nature* **2006**, 444, 347.
- [7] C. W. J. Beenakker, *Rev. Mod. Phys.* **2008**, 80, 1337.
- [8] Y. Wang, N. Xu, D. Li, J. Zhu, *Adv. Funct. Mater.* **2017**, 27, 1604134.
- [9] S. Link, S. Forti, A. Stöhr, K. Küster, M. Rösner, D. Hirschmeier, C. Chen, J. Avila, M. C. Asensio, A. A. Zakharov, T. O. Wehling, A. I. Lichtenstein, M. I. Katsnelson, U. Starke, *Phys. Rev. B* **2019**, 100, 121407.
- [10] P. Rosenzweig, H. Karakachian, D. Marchenko, K. Küster, U. Starke, *Phys. Rev. Lett.* **2020**, 125, 176403.
- [11] R. Prasher, *Science* **2010**, 328, 185.
- [12] X. Gu, Y. Wei, X. Yin, B. Li, R. Yang, *Rev. Mod. Phys.* **2018**, 90, 041002.
- [13] Y. Huang, J. Zhou, G. Wang, Z. Sun, *J. Am. Chem. Soc.* **2019**, 141, 8503.
- [14] S. Shin, Q. Wang, J. Luo, R. Chen, *Adv. Funct. Mater.* **2020**, 30, 1904815.
- [15] Y. Zhao, Y. Cai, L. Zhang, B. Li, G. Zhang, J. T. L. Thong, *Adv. Funct. Mater.* **2020**, 30, 1903929.
- [16] D. Shin, G. Wang, M. Han, Z. Lin, A. O'Hara, F. Chen, J. Lin, S. T. Pantelides, *Phys. Rev. Mater.* **2021**, 5, 044002.
- [17] Z. Tong, A. Pecchia, C. Yam, T. Dumitrică, T. Frauenheim, *Adv. Sci.* **2021**, 8, 2101624.

- [18] H. Xie, S. Hao, T. P. Bailey, S. Cai, Y. Zhang, T. J. Slade, G. J. Snyder, V. P. Dravid, C. Uher, C. Wolverton, M. G. Kanatzidis, *J. Am. Chem. Soc.* **2021**, *143*, 5978.
- [19] L. Lindsay, W. Li, J. Carrete, N. Mingo, D. A. Broido, T. L. Reinecke, *Phys. Rev. B* **2014**, *89*, 155426.
- [20] X. Gu, R. Yang, *Appl. Phys. Lett.* **2014**, *105*, 131903.
- [21] X. Gu, R. Yang, *J. Appl. Phys.* **2015**, *117*, 025102.
- [22] A. Cepellotti, *Nat. Commun.* **2015**, *6*, 6400.
- [23] A. Jain, A. J. H. McGaughey, *Sci. Rep.* **2015**, *5*, 8501.
- [24] G. Qin, Z. Qin, W.-Z. Fang, L.-C. Zhang, S.-Y. Yue, Q.-B. Yan, M. Hu, G. Su, *Nanoscale* **2016**, *8*, 11306.
- [25] T. Feng, X. Ruan, *Phys. Rev. B* **2018**, *97*, 045202.
- [26] Z. Gao, F. Tao, J. Ren, *Nanoscale* **2018**, *10*, 12997.
- [27] Z. Tong, T. Dumitrică, T. Frauenheim, *Nano Lett.* **2021**, *21*, 4351.
- [28] X. Yang, A. Jena, F. Meng, S. Wen, J. Ma, X. Li, W. Li, *Mater. Today Phys.* **2021**, *18*, 100315.
- [29] M. Bykov, T. Fedotenko, S. Chariton, D. Laniel, K. Glazyrin, M. Hanfland, J. S. Smith, V. B. Prakapenka, M. F. Mahmood, A. F. Goncharov, A. V. Ponomareva, F. Tasnádi, A. I. Abrikosov, T. Bin Masood, I. Hotz, A. N. Rudenko, M. I. Katsnelson, N. Dubrovinskaja, L. Dubrovinsky, I. A. Abrikosov, *Phys. Rev. Lett.* **2021**, *126*, 175501.
- [30] J. Wang, S. Deng, Z. Liu, Z. Liu, *Natl. Sci. Rev.* **2015**, *2*, 22.
- [31] A. Bafekry, C. Stampfl, M. Faraji, M. Yagmurcukardes, M. M. Fadlallah, H. R. Jappor, M. Ghergherehchi, S. A. H. Feghhi, *Appl. Phys. Lett.* **2021**, *118*, 203103.
- [32] B. Mortazavi, F. Shojaei, X. Zhuang, *Mater. Today Nano* **2021**, *15*, 100125.
- [33] W. Li, J. Carrete, N. A. Katcho, N. Mingo, *Comput. Phys. Commun.* **2014**, *185*, 1747.
- [34] S. Poncé, E. R. Margine, F. Giustino, *Phys. Rev. B* **2018**, *97*, 121201.
- [35] Z. Tong, S. Li, X. Ruan, H. Bao, *Phys. Rev. B* **2019**, *100*, 144306.
- [36] D. K. Efetov, P. Kim, *Phys. Rev. Lett.* **2010**, *105*, 256805.
- [37] W. Li, N. Mingo, *Phys. Rev. B* **2015**, *91*, 144304.
- [38] B. Liao, B. Qiu, J. Zhou, S. Huberman, K. Esfarjani, G. Chen, *Phys. Rev. Lett.* **2015**, *114*, 115901.
- [39] S.-Y. Yue, R. Yang, B. Liao, *Phys. Rev. B* **2019**, *100*, 115408.
- [40] *Thermal Conductivity: Theory, Properties, and Applications, Physics of Solids and Liquids* (Ed: T. M. Tritt), Kluwer Academic/Plenum Publishers, New York **2004**.
- [41] J. I. Mustafa, M. Bernardi, J. B. Neaton, S. G. Louie, *Phys. Rev. B* **2016**, *94*, 155105.
- [42] S. Li, Z. Tong, H. Bao, *J. Appl. Phys.* **2019**, *126*, 025111.
- [43] C.-H. Park, F. Giustino, M. L. Cohen, S. G. Louie, *Phys. Rev. Lett.* **2007**, *99*, 086804.
- [44] Y.-W. Tan, Y. Zhang, K. Bolotin, Y. Zhao, S. Adam, E. H. Hwang, S. Das Sarma, H. L. Stormer, P. Kim, *Phys. Rev. Lett.* **2007**, *99*, 246803.
- [45] C.-H. Park, N. Bonini, T. Sohier, G. Samsonidze, B. Kozinsky, M. Calandra, F. Mauri, N. Marzari, *Nano Lett.* **2014**, *14*, 1113.
- [46] T. Sohier, D. Campi, N. Marzari, M. Gibertini, *Phys. Rev. Mater.* **2018**, *2*, 114010.
- [47] P. B. Allen, *Phys. Rev. B* **1978**, *17*, 3725.
- [48] F. J. Pinski, P. B. Allen, W. H. Butler, *Phys. Rev. B* **1981**, *23*, 5080.
- [49] G. W. Ludwig, R. L. Watters, *Phys. Rev.* **1956**, *101*, 1699.
- [50] J. Qiao, *Nat. Commun.* **2014**, *5*, 4475.
- [51] W.-B. Zhang, Q. Qu, K. Lai, *ACS Appl. Mater. Interfaces* **2017**, *9*, 1702.
- [52] V. K. Yadav, *Phys. B: Condens. Matter* **2019**, *571*, 291.
- [53] S. H. Mir, V. K. Yadav, J. K. Singh, *ACS Omega* **2020**, *5*, 14203.
- [54] W. Cai, A. L. Moore, Y. Zhu, X. Li, S. Chen, L. Shi, R. S. Ruoff, *Nano Lett.* **2010**, *10*, 1645.
- [55] A. J. Gabourie, S. V. Suryavanshi, A. B. Farimani, E. Pop, *2D Mater.* **2020**, *8*, 011001.
- [56] G. D. Mahan, *Many-Particle Physics*, Kluwer Academic/Plenum Publishers, New York, NY **2000**.
- [57] G. Kresse, J. Hafner, *Phys. Rev. B* **1993**, *47*, 558.
- [58] J. P. Perdew, K. Burke, M. Ernzerhof, *Phys. Rev. Lett.* **1996**, *77*, 3865.
- [59] T. Feng, X. Ruan, *Phys. Rev. B* **2016**, *93*, 045202.
- [60] Z. Tong, X. Yang, T. Feng, H. Bao, X. Ruan, *Phys. Rev. B* **2020**, *101*, 125416.
- [61] P. Giannozzi, S. Baroni, N. Bonini, M. Calandra, R. Car, C. Cavazzoni, D. Ceresoli, G. L. Chiarotti, M. Cococcioni, I. Dabo, A. Dal Corso, S. de Gironcoli, S. Fabris, G. Fratesi, R. Gebauer, U. Gerstmann, C. Gougoussis, A. Kokalj, M. Lazzeri, L. Martin-Samos, N. Marzari, F. Mauri, R. Mazzarello, S. Paolini, A. Pasquarello, L. Paulatto, C. Sbraccia, S. Scandolo, G. Sclauzero, A. P. Seitsonen, et al., *J. Phys.: Condens. Matter* **2009**, *21*, 395502.
- [62] N. Troullier, J. L. Martins, *Phys. Rev. B* **1991**, *43*, 1993.
- [63] J. Noffsinger, F. Giustino, B. D. Malone, C.-H. Park, S. G. Louie, M. L. Cohen, *Comput. Phys. Commun.* **2010**, *181*, 2140.
- [64] S. Poncé, E. Margine, C. Verdi, F. Giustino, *Comput. Phys. Commun.* **2016**, *209*, 116.
- [65] Z. Tong, H. Bao, *Int. J. Heat Mass Transfer* **2018**, *117*, 972.
- [66] S. Li, Z. Tong, X. Zhang, H. Bao, *Phys. Rev. B* **2020**, *102*, 174306.